(Received 26 November 2025, Accepted 22 December 2025, Scheduled 27 January 2026)

A Hybrid Quantum Transport Simulator for MOSFETs Using Non-Equilibrium Green's Function and FDTD

Kai Ren*

Department of Electrical Engineering and Computer Science
South Dakota School of Mines and Technology, Rapid City, SD 57701, USA

ABSTRACT: Based on the time-dependent Schrödinger equation, a finite-difference time-domain (FDTD) method is proposed to investigate electron propagation with the presence of tunneling potential distributions in metal-oxide-semiconductor field-effect transistors (MOSFETs). The channel current equation in the drift-diffusion model for classical transport is derived from the probability current formula with a plane wave assumption of the electron's state function. In both classical and quantum regimes, channel currents are numerically simulated based on quantum transport in MOSFETs using transmission functions and Fermi-Dirac distributions. The transmission function is obtained from the non-equilibrium Green's function (NEGF), indicating the probability of electrons through a channel. To determine the number of electrons at both source and drain terminals of a MOSFET, the Fermi-Dirac distributions are calculated. Numerical simulations of channel currents with various external gate-source and drain-source voltages are investigated, showing that a similar peak channel current can be generated with lower external voltages in a smaller MOSFET with a shorter gate length. Electron forward and backward propagations are obtained through FDTD simulations to demonstrate the difference of cutoff modes in classical and quantum MOSFETs.

1. INTRODUCTION

Moore's law has been a driving force behind the rapid development of the semiconductor industry since 1965 [1]. It predicts the increasing trend of the number of components, doubling per integrated circuit per year, which was revised to doubling every two years in 1975 [2]. However, the doubling trend has slowed down in the recent five years, due to the size of each transistor approaching the quantum regime (nanometer range). It is of importance to understand fundamental physics and consider the wave nature of electrons in semiconductors, which has been investigated [3–13].

In early works [3–5], the quantum tunneling effects of electrons through insulating gate oxide and resonant tunneling through inversion layers between drain and source terminals have been explored. In [6], metal-semiconductor field-effect transistors (MESFETs) were simulated based on quantum moment equations due to the gate length approaching the quantum length. In [7–9], hybrid classical and quantum drift-diffusion models have been developed for simulating semiconductors numerically. In [10], a fully quantum method was applied to study the Schottky-barrier tunnel transistor with a channel length as short as 5 nm. In [11, 12], metal-oxide-semiconductor field-effect transistors (MOSFETs) used for quantum computing were characterized by a semiconductor device analyzer at extremely low temperatures, where quantum transport in 40-nm and 55-nm MOSFETs was verified experimentally. In [13], a comprehensive review of quantum transport has been carried out to promote the implementation of quantum techniques into the future development of semiconductor devices.

In quantum transport, the non-equilibrium Green's function (NEGF) has been applied to obtain a transmission matrix when electrons tunneling through a transistor's channel [13–36]. In [14], to guarantee the conservation laws of particle number, momentum, angular momentum, and energy, a NEGF approach was used to observe a transport process in a many-particle system. Most modern methods of solving quantum transport in semiconductor devices were based on [15], where a generalized Green's function was proposed in the matrix form. However, this approach assumed that the Hamiltonian was always Hermitian, which fails with the presence of self-energies. Based on Kadanoff and Baym's work [15], NEGF was applied to both correlated and noncorrelated initial states of a system and extended to the Boltzmann equation [16]. In [17], to obtain currents flowing through a region of interests, a Landauer formulation was developed with and without considering electron interactions using NEGF and equilibrium Green's function (EGF), respectively. Current-voltage (IV) characteristics, transconductance, and full quantum-mechanical simulations of double-gate MOSFETs were explored based on NEGF [18–20]. In [18], quantum transport was studied in 2D n-channel MOSFETs using real and mode-space approaches with NEGF. In [19], high transconductance close to the theoretical ballistic limit has been achieved in a MOSFET with a 10 nm channel length. In [20], the leakage current and drain conductance were reduced using a silicon-on-insulator MOSFET with the help of NEGF analysis. Beyond double-gate MOSFETs, quantum transport has been investigated in FinFETs us-

* Corresponding author: Kai Ren (kai.ren@sdsmt.edu).

ing NEGF [21–24]. In [21], a 3D quantum transport simulator was explored to show a better performance of the trigate FinFET based on the contact block reduction method. In [22], silicon FinFETs with a channel length of 60 nm were simulated with a Nano-electronic Modeling Tool NEMO 3D and fabricated to present the control of the gate potential over the degree of hybridization of the electron wavefunction with experimental characterizations. In [23], phonon scattering in nanowires and FinFETs with different cores was investigated with the NEGF formulation. In [24], full quantum simulations of a 10 nm FinFET with high dielectric spacers were studied to achieve the reduction of the leakage current and improvement of the short-channel effects. Tunnel field-effect transistors (TFETs) using nanoribbons and heterojunctions were investigated using NEGF [25, 26]. In [27], a new Nano-electronic Simulation Software (NESS) with three different solvers: a Kubo-Greenwood, drift-diffusion, and NEGF was proposed to simulate nanoscale transistors. In [28–31], self-consistent Schrödinger-Poisson methods were considered in the numerical simulations. In [32, 33], hybrid simulators using the GPU acceleration and combination with conventional TCAD software were implemented, respectively. In [34, 35], quantum-classical modeling has been utilized, where quantum transport methods captured confinement and tunneling in the channel, while electrostatics and surrounding device regions were treated with classical or semiclassical models for computational efficiency. However, in the above quantum transport analysis, electron scattering through a transistor channel cannot be observed in the time domain to understand the channel current formation.

Finite-difference time-domain (FDTD) simulations of quantum devices based on the Schrödinger equation have been investigated independently from the quantum transport community [37–46]. In [37], a staggered-time algorithm was applied to observe electron wave packet scattering in a square quantum well. In [38, 39], eigenfunctions of 2D quantum dots and 3D arbitrary quantum well were constructed using the FDTD method. In [40], the convergence and stability of the FDTD approach were analyzed based on a 2D quantum well. In [41], wavefunction scattering through a narrow potential barrier was investigated using the time-domain method. In [42], 3D FDTD approach was presented for accurately calculating the eigenenergies and eigenfunctions of quantum wires without approximating the Schrödinger equation, demonstrating agreement with analytical solutions for cylindrical wires and efficiency suitable for complex nanostructure simulations. In [43], both second- and higher-order FDTD algorithms were developed for solving the Schrödinger equation on a nonuniform grid, deriving stability bounds for larger time steps and demonstrating through numerical tests that the higher-order scheme and nonuniform gridding improve accuracy and reduce dispersion errors of a particle in a harmonic oscillator. In [44], the FDTD method was investigated to derive accurate expressions for numerical probability, energy, and flux that satisfy conservation laws in infinite wells, potential barriers, and proton tunneling. In [45], a spectral element time-domain (SETD) method with perfectly matched layers (PML) was presented for solving the 3D Schrödinger equation, achieving spectral accuracy and computational efficiency through Gauss-Lobatto-Legendre polynomials and diagonal mass matrices in quantum waveguides, T-stub structures, and resonant tunneling diodes. In [46], critical-point-based stability analyses of the FDTD method were provided for the 3D Schrödinger equation with both vector and scalar potentials, deriving comprehensive stability conditions validated by numerical experiments and demonstrating their effectiveness for simulating quantum-electromagnetic interactions. In [47], electron-wavefunction propagation was studied in MOSFETs. Different quantum structures were simulated using FDTD based on the Schrödinger equation. However, FDTD analyses of electron scattering through a MOSFET channel and the connection with IV characteristics obtained from the NEGF formalism in quantum transport were not investigated. To the best of the author's knowledge, such a connection has not been achieved in open literature.

Contributions: In this paper, a hybrid quantum simulator is developed to combine FDTD and NEGF methods for connecting electron scattering through transistor channels to IV characteristics of the transistors. This bridges the two independent scientific communities for a better understanding of nanoscale transistors. The simulator is described as a hybrid in the sense that it integrates distinct physical modeling frameworks — quantum transport and field-based representations — within a unified simulation workflow using NEGF and FDTD. Under the assumption of no concentration gradients, the classical drift-diffusion model is derived directly from the Schrödinger equation. Channel currents in quantum mechanical MOSFETs are derived based on the transmission function and Fermi-Dirac distributions, where the NEGF is used to represent the electron transmission probability through the channel. IV characteristics of MOSFETs with different channel lengths of 20 nm and 200 nm are obtained under the condition of various drain-source and gate-source voltages. Observe that when a MOSFET is in the cutoff mode (no channel currents) with a channel length of 200 nm, there would be channel currents in another MOSFET with a shorter channel length of 20 nm under the same low gate-source voltages. To explain this observation and understand the essence of MOSFET operations, FDTD simulations of electron propagating through MOSFET channels are performed. It is investigated that the potential distributions across the channel are different in MOSFETs with the same external gate-source and drain-source voltages but different channel lengths. A longer channel will result in electron backward propagation with the presence of the potential barrier, leading to the cutoff mode. There will be electrons forward propagating through the potential barrier with a shorter channel, indicating currents flowing through the channel.

Section 2 shows the derivation of the drift-diffusion model in classical transport, obtained directly from the Schrödinger equation. Quantum transport and IV characteristics in MOSFETs using the Green's function are presented in Section 3. Section 4 describes electron propagations with the presence of potential barriers in MOSFETs' channels through the FDTD numerical method. In Section 5, the simulations of MOSFETs based on the Green's function and FDTD are provided to demonstrate the difference in classical and quantum transport with various external voltages. Conclusions are shown in the last Section 6.

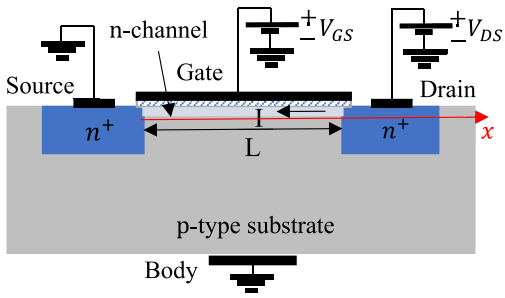

FIGURE 1. An n-channel enhancement metal-oxide-semiconductor field-effect transistor (NMOS) with a channel length of L. The gate and drain terminals are connected to external DC power supplies V_{GS} and V_{DS}. The source and body terminals are grounded. Assume that there is no diffusion and that the channel length approximately equals the gate length.

2. CLASSICAL TRANSPORT

Classical transport will be obtained from the Schrödinger equation in this section, which is an intermediate step of quantum transport derivation. In the microscopic regime, the wave nature of an electron rather than a particle is investigated in nanoscale quantum-mechanical systems. Fig. 1 shows a 1D n-channel enhancement metal-oxide-semiconductor field-effect transistor (NMOS) with a channel length of L, placed along the x axis. Assume that there are no concentration gradients, resulting in no diffusion length. The channel and gate lengths are assumed to be identical. When a channel is formed, the channel current I is flowing from the drain to the source terminal, resulting from the opposite moving direction of electrons along the $+x$ axis. For an electron with a charge $Q(x,t)$ and a wavefunction $\psi(x,t)$ in the confined 1D channel, the channel current I is given by the time change rate of the charge [36],

$$I = \frac{\partial Q(x,t)}{\partial t} = -q \int \frac{\partial}{\partial t} \left|\psi\left(x,t\right)\right|^2 dx \tag{1}$$

where the elementary charge $q = 1.602 \times 10^{-19}$ C, and the change rate of the wavefunction with respect to time is,

$$\frac{\partial}{\partial t} \left|\psi\left(x,t\right)\right|^2 = \psi^* \frac{\partial \psi}{\partial t} + \frac{\partial \psi^*}{\partial t} \psi \tag{2}$$

where $*$ denotes the complex conjugate, leading to the involvement of the 1D time-dependent Schrödinger equation [36],

$$i\bar{h} \frac{\partial}{\partial t} \psi\left(x,t\right) = \left[-\frac{\bar{h}^2}{2m_e} \frac{\partial^2}{\partial x^2} + V\left(x\right)\right] \psi(x,t) \tag{3}$$

where the reduced Planck's constant $\bar{h} = \frac{h}{2\pi} = 6.582 \times 10^{-16}$ eV $\cdot$ s (eV denotes electron volt), the mass of an electron $m_e = 9.109 \times 10^{-31}$ kg, and V is the potential distribution in the channel. Rearranging (3), finding expressions for $\frac{\partial \psi}{\partial t}$ and its complex conjugate term $\frac{\partial \psi^*}{\partial t}$, and substituting back to (2), we have,

$$\frac{\partial}{\partial t} \left|\psi\left(x,t\right)\right|^2 = \frac{\partial}{\partial x} \left[\frac{i\bar{h}}{2m_e} \left(\frac{\partial \psi^*}{\partial x} \psi - \psi^* \frac{\partial \psi}{\partial x}\right)\right] = \frac{\partial}{\partial x} J(xt) \tag{4}$$

where the probability current is defined as $J(x,t) \equiv \frac{i\bar{h}}{2m_e} \left(\frac{\partial \psi^*}{\partial x} \psi - \psi^* \frac{\partial \psi}{\partial x}\right)$. Substituting (4) into (1), the channel current can be expressed as,

$$I = -qJ(x,t) \tag{5}$$

Assume that there are no concentration gradients and that the electron wavefunction is a uniform plane wave, propagating through the channel in the $+x$ direction,

$$\psi\left(x,t\right) = \mathrm{C} e^{i(kx+\omega t)} \tag{6}$$

where C is the amplitude, k the wavenumber, and ω the angular frequency of the wavefunction. Note that i instead of $-j$ is used to follow the conventional notation in quantum mechanics. Plugging (6) into the probability current equation, it is obtained that,

$$J\left(x,t\right) = \frac{\bar{h}k}{m_e} \left|\psi\left(x,t\right)\right|^2 = \mu_e E n\left(x,t\right) \tag{7}$$

where the relationship between the momentum of a wavefunction and a particle in quantum mechanics $\bar{h}k = m_e v$ is applied. The electron velocity $v = \mu_e E$, where μ_e is the electron mobility, and E is the electric field intensity across the channel. The effective 1D electron density of the MOSFET channel is defined as $n(x,t) = |\psi(x,t)|^2$ with a unit of m^{-1}. Therefore, substituting (7) into (5), the continuous formulation of the channel current of the drift-diffusion model in classical transport without concentration gradients can be written as,

$$I = -q\mu_e E n\left(x,t\right) \tag{8}$$

Dropping the time harmonic convention $e^{i\omega t}$, (8) can be rewritten as,

$$I = -q\mu_e E n\left(x\right) \tag{9}$$

where $n(x)$ has the same unit as $n(x,t)$, which is m^{-1}. This equation is commonly used to obtain IV characteristics of MOSFETs in classical electronic circuits.

3. QUANTUM TRANSPORT

Channel currents represented by the transmission matrix and Fermi-Dirac distributions in quantum transport will be derived, which is used to investigate electron behavior under quantum mechanical effects in semiconductor devices [36]. The discretized representation of the channel current flowing through a cell with a width of Δx in a nanoscale semiconductor is represented by,

$$I_{cell} = -q \frac{v}{\Delta x} n\left(x\right) \tag{10}$$

In the quantum regime, it is important to identify the electron density $n(x)$, which is obtained from the diagonal of the density matrix $\rho(x,x')$,

$$n\left(x\right) = \rho\left(x,x\right) = \frac{1}{2\pi} \mathrm{Tr} \left[\int_{-\infty}^{\infty} dE f_F\left(E-\mu\right) A\left(x,x;E\right)\right] \tag{11}$$

where Tr is the trace operator, and the Fermi-Dirac distribution for a single-energy channel is a function of energy E,

$$f_F\left(E-\mu\right)=\frac{1}{1+e^{\left(\frac{E-\mu}{k_BT}\right)}} \tag{12}$$

where μ is the Fermi level (chemical potential) in the semiconductor, the Boltzmann constant $k_B=1.38\times10^{-23}$ J/K, and T is the temperature in Kelvin. The spectral function A is defined as,

$$A(x,x;E)=2\pi\sum\nolimits_m\phi_m\left(x\right)\delta(E-\varepsilon_m)\phi_m^*\left(x\right) \tag{13}$$

where ϕ_m is the mth eigenstate, and ε_m is the corresponding eigenenergy of an electron in a semiconductor device. The spectral function A is a diagonal matrix, which can be represented by the Green's function [36],

$$A\left(E\right)=i\left[G\left(E\right)-G^{\dagger}\left(E\right)\right] \tag{14}$$

where $\dagger$ denotes the Hermitian conjugate (complex conjugate transpose), and the real space Green's function with a loss term self-energy matrix Σ is a function of energy E as well,

$$G\left(E\right)=\left[IE-H-\Sigma\right]^{-1} \tag{15}$$

where -1 denotes the inverse of a matrix, I the identity matrix, and H the Hamiltonian matrix, which is obtained from the 1D time-independent Schrödinger equation [36],

$$E\psi\left(x\right)=H\psi\left(x\right)=\left[-\frac{\hbar^2}{2m_e}\frac{\partial^2}{\partial x^2}+V\left(x\right)\right]\psi\left(x\right) \tag{16}$$

leading to the Hamiltonian matrix $H=-\frac{\hbar^2}{2m_e}\frac{\partial^2}{\partial x^2}+V(x)$. The self-energy matrix Σ in (15) is introduced into the Green's function to add loss terms at both sides of the NMOS channel, connecting the channel to external reservoirs. The source and drain contacts are modeled using energy-dependent, mode-matched self-energies derived from semi-infinite effective-mass leads, ensuring reflectionless open boundary conditions for propagating modes within the contact band. There are nonzero complex numbers only at the corners of the sparse matrix Σ, which is obtained by the finite-difference time-domain (FDTD) representation,

$$\Sigma=-\chi_0\begin{bmatrix}e^{i\cdot k_1\Delta x} & \cdots & 0\\ \vdots & \ddots & \vdots\\ 0 & \cdots & e^{i\cdot k_2\Delta x}\end{bmatrix} \tag{17}$$

where the constant $\chi_0=\frac{\hbar^2}{2m_e\Delta x^2}$, and k_1 and k_2 are wavenumbers at left and right edges of the NMOS channel in Fig. 1, which can be obtained from the relation between the energy level and corresponding potentials $E=\frac{(\hbar k)^2}{2m_e}+V(x)$. Thus, the wavenumber $k_{1,2}$ can be expressed by,

$$k_{1,2}=\frac{\sqrt{2m_e(E-V_{1,2})}}{\hbar} \tag{18}$$

where $V_{1,2}$ are different potentials at the left and right edges of the NMOS channel. From the self-energy matrix Σ, a broadening matrix Γ is used to couple a quantum system to external reservoirs, defined as,

$$\Gamma=i\left[\Sigma-\Sigma^{\dagger}\right] \tag{19}$$

The broadening matrix Γ is used to obtain the spectral function A without performing eigenvalue decompositions. Substituting (17) to (19) with a small $k\Delta x$ approximation, one can find that,

$$\Gamma=\begin{bmatrix}\frac{\hbar v_1}{\Delta x} & \cdots & 0\\ \vdots & \ddots & \vdots\\ 0 & \cdots & \frac{\hbar v_2}{\Delta x}\end{bmatrix} \tag{20}$$

where $v_{1,2}$ are corresponding electron velocities at the left and right edges of the NMOS channel, which can be obtained from the wavenumbers in (18), leading to $v_{1,2}=\frac{\hbar k_{1,2}}{m_e}$. Multiplying (14) from the left and right by G^{-1} and $\left(G^{\dagger}\right)^{-1}$, respectively, using the relation $\left(G^{\dagger}\right)^{-1}=\left(G^{-1}\right)^{\dagger}$ and real elements in $[IE-H]$ matrix, the spectral matrix can be rewritten as,

$$A=G\Gamma G^{\dagger} \tag{21}$$

where the spectral function can be separated into the addition of two spectral functions at two sides of the channel $A=A_1+A_2$, and Γ is the broadening matrix in (19) and (20). In practice, the spectral matrix is calculated based on (21) instead of (13), due to the removal of additional mathematical burdens in the eigenvalue decompositions.

By multiplying the broadening matrix Γ at both sides of the electron density function (11) and using the relation in (20), we obtain

$$\frac{\hbar v}{\Delta x}n\left(x\right)=\frac{1}{2\pi}\mathrm{Tr}\left[\int_{-\infty}^{\infty}dE\cdot f_F\left(E-\mu\right)\Gamma(E)A\left(x,x;E\right)\right] \tag{22}$$

where v and μ could be different electron velocities and Fermi levels at the left and right edges of the NMOS channel. Therefore, currents flowing into the channel at the source side I_1 and out of the channel at the drain side I_2 can be obtained from (10) and (22) [36],

$$I_1=-\frac{q}{2\pi\hbar}\mathrm{Tr}\left[\int_{-\infty}^{\infty}dE\cdot f_F\left(E-\mu_1\right)\Gamma_1(E)A(x,x;E)\right] \tag{23a}$$

$$I_2=-\frac{q}{2\pi\hbar}\mathrm{Tr}\Bigg[\int_{-\infty}^{\infty}dE\cdot\Gamma_1(E)\Big[f_F\left(E-\mu_1\right)A_1\left(x,x;E\right)+f_F\left(E-\mu_2\right)A_2\left(x,x;E\right)\Big]\Bigg] \tag{23b}$$

Define the integrands as the current flow per energy at the two sides of the channel, leading to,

$$\tilde{I}_1 = \mathrm{Tr}\left[\Gamma_1 f_1(A_1+A_2)\right] \tag{24a}$$

$$\tilde{I}_2 = \mathrm{Tr}\left[\Gamma_1(f_1A_1+f_2A_2)\right] \tag{24b}$$

where the spectral function $A_1=G\Gamma_1G^{\dagger}$ and $A_2=G\Gamma_2G^{\dagger}$. The Fermi-Dirac distribution at the left source side in Fig. 1 is

$f_1 = f_F(\varepsilon_0 - \mu_1)$. Due to the presence of the external DC voltage supply V_{DS} at the right drain side, its Fermi-Dirac distribution $f_2 = f_F(\varepsilon_0 - \mu_2) = f_F(\varepsilon_0 - \mu_1 + qV_{DS})$. With several steps of rearrangement, the total current per energy on the left side of the channel is defined by,

$$\tilde{I} = \tilde{I}_1 - \tilde{I}_2 = \mathrm{Tr}\left[\Gamma_1 G \Gamma_2 G^\dagger\right](f_1 - f_2) \tag{25}$$

Therefore, the channel current flowing from the drain to the source in Fig. 1 is,

$$I = \frac{q}{2\pi\hbar}\int_{-\infty}^{\infty} dE \cdot \tilde{I} = \frac{q}{2\pi\hbar}\int_{-\infty}^{\infty} dE \cdot T(E)(f_1 - f_2) \tag{26}$$

where the transmission function $T(E) = \mathrm{Tr}\left[\Gamma_1 G \Gamma_2 G^\dagger\right]$, which is the probability that an electron crosses the channel as a function of energy. The channel current in a MOSFET can be obtained from the transmission function and Fermi-Dirac distributions without eigenvalue decompositions of electron wavefunctions. IV characteristics of field-effect transistors (FETs) with different external DC gate-source and drain-source voltages V_{GS} and V_{DS} can be obtained from (26). The NEGF solver of the hybrid algorithm to obtain IV characteristics is presented as follows.

1. Initialize all parameters, such as channel length, cell size, the reduced Planck's constant, and electron mass.
2. For each external drain-source (V_{DS}) or gate-source (V_{GS}) voltage:
   a. Build a Tunneling barrier potential V using (38b).
   b. Construct the Hamiltonian matrix H using (38a) and (38b).
   c. Calculate Fermi-Dirac distribution functions f_1 and f_2 as a function of energy.
   d. For each energy level:
      i. Compute the self-energy matrix Σ and the broadening matrix Γ using (17) and (20).
      ii. Calculate the Green's function matrix G using (15).
      iii. Compute the transmission matrix $T(E) = \mathrm{Tr}\left[\Gamma_1 G \Gamma_2 G^\dagger\right]$.
   e. Obtain the channel current I by integrating over energy E based on (26).

4. ELECTRON SCATTERING USING FDTD

Even though IV characteristics of FETs can be obtained from (26), it might be difficult to understand the behavior of transistors with different channel lengths but the same external voltages. This section focuses on understanding electron propagation with the presence of different potential distributions in channels of transistors, using the FDTD method. Rearranging the 1D time-dependent Schrödinger equation (3), we have,

$$\frac{\partial}{\partial t}\psi(x,t) = \frac{i\hbar}{2m_e}\frac{\partial^2\psi(x,t)}{\partial x^2} - \frac{i}{\hbar}V(x)\psi(xt) \tag{27}$$

The complex-valued wavefunction can be separated into the real and imaginary components ψ_{real} and ψ_{imag}, leading to two coupled equations,

$$\frac{\partial\psi_{real}(x,t)}{\partial t} = -\frac{\hbar}{2m_e}\frac{\partial^2\psi_{imag}(x,t)}{\partial x^2} + \frac{1}{\hbar}V(x)\psi_{imag}(x,t) \tag{28a}$$

$$\frac{\partial\psi_{imag}(x,t)}{\partial t} = \frac{\hbar}{2m_e}\frac{\partial^2\psi_{real}(x,t)}{\partial x^2} - \frac{1}{\hbar}V(x)\psi_{real}(x,t) \tag{28b}$$

Observe that the real and imaginary components of electron wavefunctions are coupled. Note that the left-hand side of the above equations is the first order partial derivative with respect to time t and that the first term on the right-hand side is the second-order partial derivative with respect to x. Using the FDTD algorithm, the first order time derivative and second-order spatial derivative can be written as,

$$\frac{\partial\psi(x,t)}{\partial t} = \frac{\psi^{m+1}(n) - \psi^m(n)}{\Delta t} \tag{29a}$$

$$\frac{\partial^2\psi(x,t)}{\partial x^2} = \frac{\psi^{m+1/2}(n+1) - 2\psi^{m+1/2}(n) + \psi^{m+1/2}(n-1)}{\Delta x^2} \tag{29b}$$

where ψ can represent either ψ_{real} or ψ_{imag}; m and Δt are the index and step size in the time domain; and n and Δx are the index and step size in the spatial domain. One can obtain that $\psi^m(n) = \psi(n\cdot\Delta x, m\cdot\Delta t)$ with integers $n = 1:N$ and $m = 1:M$, where M is the total number of discretized cells in the time domain, and N is the total number of discretized spatial cells of the channel in a MOSFET. Substitute (29a) and (29b) into (28a) and (28b) with several steps of rearrangements, the FDTD representation of the 1D time-dependent Schrödinger equation is obtained,

$$\psi_{real}^{m+1}(n) = \psi_{real}^{m}(n) - \frac{\hbar}{2m_e}\frac{\Delta t}{\Delta x^2}\left[\psi_{imag}^{m+1/2}(n+1) - 2\psi_{imag}^{m+1/2}(n) + \psi_{imag}^{m+1/2}(n-1)\right] + \frac{\Delta t}{\hbar}V(n)\psi_{imag}^{m+1/2}(n) \tag{30a}$$

$$\psi_{imag}^{m+3/2}(n) = \psi_{imag}^{m+1/2}(n) + \frac{\hbar}{2m_e}\frac{\Delta t}{\Delta x^2}\left[\psi_{real}^{m+1}(n+1) - 2\psi_{real}^{m+1}(n) + \psi_{real}^{m+1}(n-1)\right] - \frac{\Delta t}{\hbar}V(n)\psi_{real}^{m+1}(n) \tag{30b}$$

Note that the imaginary parts of ψ in the time domain are shifted by half a discretized cell in the numerical domain of

interest. To maintain stability in the FDTD simulation of an electron in a MOSFET, two conditions must be satisfied, which are conventionally chosen as $\frac{\hbar}{2m_e}\frac{\Delta t}{(\Delta x)^2} < 0.15$ and $\frac{\Delta t \cdot V(n)}{\hbar} < 0.15$. The FDTD solver of the hybrid algorithm to obtain electron propagation in a MOSFET is shown as follows.

1. Initialize all parameters, such as channel length, cell size, time step size, the reduced Planck's constant, electron mass, drain-source and gate-source voltages, etc.
2. Build a Tunneling barrier potential V using (38b).
3. Initialize a normalized electron wavefunction.
4. For each time step m:
   a. For each spatial step n:
      i. Update the real component of the wavefunction $\psi_{real}^{m+1}(n)$ using (30a).
      ii. Update the imaginary component of the wavefunction $\psi_{imag}^{m+3/2}(n)$ using (30b).

Figure 2 shows the flowchart of the proposed hybrid quantum transport algorithm using NEGF and FDTD, which shares the same steps of initializing parameters and constructing the tunneling barrier potential. In the parameter initialization, drain-source and gate-source voltages are specified, and one corresponding channel current will be the output after running the algorithm. To obtain IV characteristics of the MOSFETs, different values of drain-source and gate-source voltages are simulated.

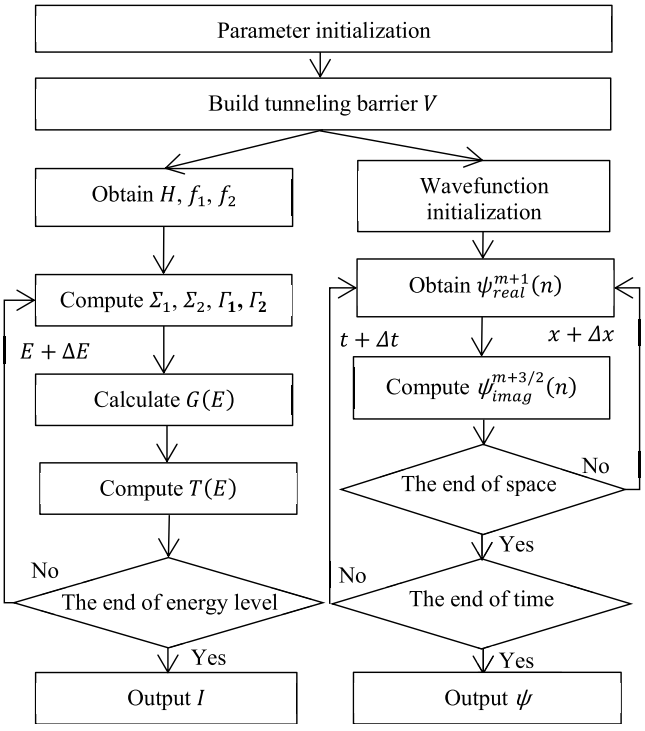

FIGURE 2. Flowchart of the proposed hybrid quantum transport algorithm.

5. NUMERICAL SIMULATIONS

As a simulation example, IV characteristics of NMOS with different channel lengths of 200 nm and 20 nm are investigated through the transmission function calculations with the Green's function. To understand the channel current formation, electron forward and backward propagations with the presence of channel potential barriers are studied by FDTD simulations. Assume that the tunneling barrier potential is distributed in 200-nm and 20-nm channels of silicon based NMOS. There is a local effect of the potential distribution on the drain side with the external DC voltage source V_{DS}. To reduce the complexity of a fully self-consistent solution using Poisson-Schrödinger simulations and have a better focus on the qualitative analysis of quantum transport mechanisms, a fixed trapezoidal potential barrier across the MOSFET channel is assumed to be an effective potential in both NEGF and FDTD simulations.

5.1. IV Characteristics Using the NEGF Solver

Let us first consider both 200-nm and 20-nm NMOS with external drain and gate terminals connected to the ground, where the channel lengths are 200 nm and 20 nm, respectively. There will be no current flowing through the channels. The simulation model excludes several physical effects, including phonon and impurity scattering, mobility and relaxation processes, many-body interactions beyond mean-field electrostatics, and degeneracy effects beyond Fermi-Dirac statistics at the contacts. Table 1 shows the parameters for NEGF and FDTD simulations. Fig. 3(a) shows the trapezoid-shaped tunneling barrier potential distribution V of the 200-nm NMOS when the external drain-source and gate-source voltages $V_{GS} = 0\,\text{V}$ and $V_{DS} = 0\,\text{V}$. The peak potential barrier is assumed to be 0.7 eV, since the NMOS is assumed to be silicon-based.

TABLE 1. Simulation parameters.

Device length [nm]	200	20
Δx [nm]	0.05	0.05
Δt [as] (attosecond)	5	5
Effective Mass	0.25	0.25
Temperature [K]	290	290
Energy Grid Limits	[0, 1]	[0, 1]
Energy Step	0.004	0.004
Source Chemical Potentials [eV]	0.5	0.5
Drain Chemical Potentials [eV]	$0.5 - qV_{DS}$	$0.5 - qV_{DS}$

Figure 3(b) presents the transmission function $T(E) = \text{Tr}\left[\Gamma_1 G \Gamma_2 G^\dagger\right]$. The transmission is 0 when the normalized energy level is less than approximately 0.7, showing that the electrons without enough energy cannot pass through the channel. Assume that the Fermi level (chemical potential) at the source $\mu_1 = 0.5\,\text{eV}$. Fig. 3(c) presents the Fermi-Dirac distributions on both sides of the NMOS, which are identical due to $V_{DS} = 0\,\text{V}$. Figs. 4(a), 4(b), and 4(c) describe the trapezoid-shaped tunneling barrier potential distribution V, the transmission function T, and the Fermi-Dirac distributions of a shorter

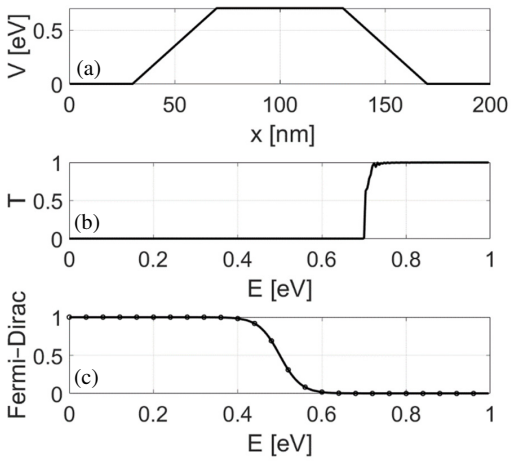

FIGURE 3. (a) The tunneling potential distribution, (b) transmission matrix, and (c) Fermi-Dirac functions in a silicon-based NMOS channel with a length of 200 nm. The external drain-source and gate-source voltages $V_{GS} = 0$ V and $V_{DS} = 0$ V. Assume that the barrier potential is 0.7 eV.

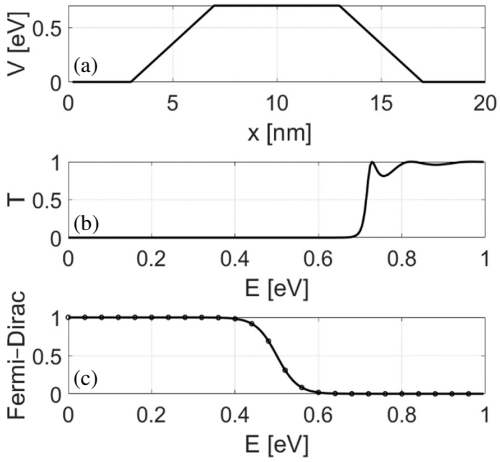

FIGURE 4. (a) The tunneling potential distribution, (b) transmission matrix, and (c) Fermi-Dirac functions in a silicon-based NMOS channel with a length of 20 nm. The external drain-source and gate-source voltages $V_{GS} = 0$ V and $V_{DS} = 0$ V. Assume that the barrier potential is 0.7 eV.

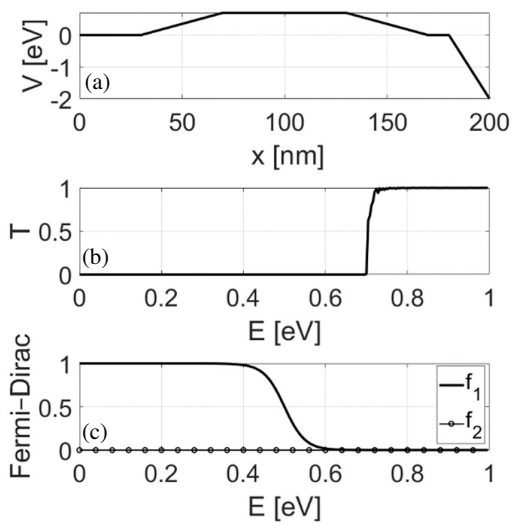

FIGURE 5. (a) The tunneling potential distribution, (b) transmission matrix, and (c) Fermi-Dirac functions in a silicon-based NMOS channel with a length of 200 nm. The external drain-source and gate-source voltages $V_{GS} = 0$ V and $V_{DS} = 2$ V. Assume that the barrier potential is 0.7 eV.

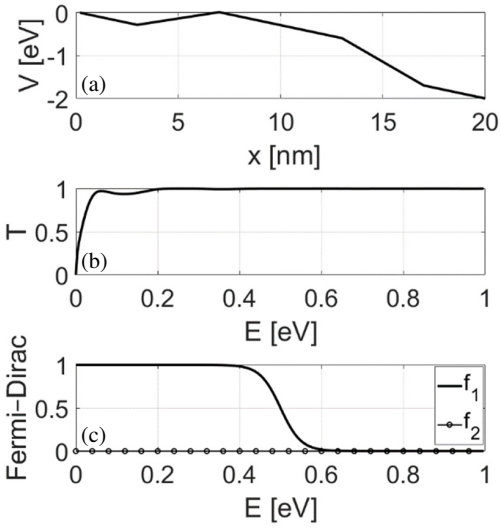

FIGURE 6. (a) The tunneling potential distribution, (b) transmission matrix, and (c) Fermi-Dirac functions in a silicon-based NMOS channel with a length of 20 nm. The external drain-source and gate-source voltages $V_{GS} = 0$ V and $V_{DS} = 2$ V. Assume that the barrier potential is 0.7 eV.

20-nm NMOS. Compared to Figs. 3(a) and 3(c), a similar potential distribution and the same Fermi-Dirac distributions are obtained. Due to the difference in channel length, a different transmission function is obtained in Fig. 4(b).

Different from the simulation scenarios in Figs. 3 and 4, an external DC voltage source $V_{DS} = 2$ V is connected to the drain terminal while keeping other parameters unchanged. Figs. 5 and 6 present the trapezoid-shaped tunneling barrier potential distribution V, the transmission function T, and the Fermi-Dirac distributions of NMOS with different channel lengths. Compared with Figs. 3 and 5, the potential distribution at the drain side is changed due to the assumed local effect of the 2 V voltage source. The transmission function is nearly unchanged due to the unchanged barrier potential. The Fermi-Dirac distribution f_2 at the drain side is reduced to approximately 0 because of the 2 V external voltage source. Compared with Figs. 4 and 6, the potential distribution across the entire channel in Fig. 6 is changed, due to the short channel length of 20 nm. This leads to a decrease in the required electron energy to pass through the channel and generate currents, as shown in Fig. 6(b). Compared with Figs. 5 and 6, the potential distributions and transmission functions might be totally different when only the sizes of the NMOS are different but other parameters are the same.

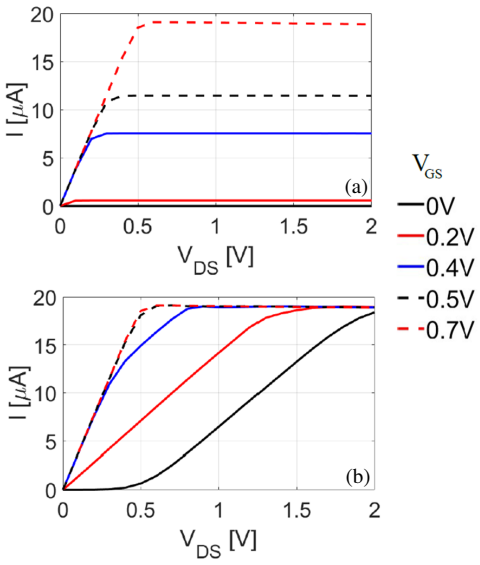

FIGURE 7. IV characteristics of a silicon-based NMOS as a function of V_{GS} and V_{DS} with different channel lengths of (a) 200 nm and (b) 20 nm.

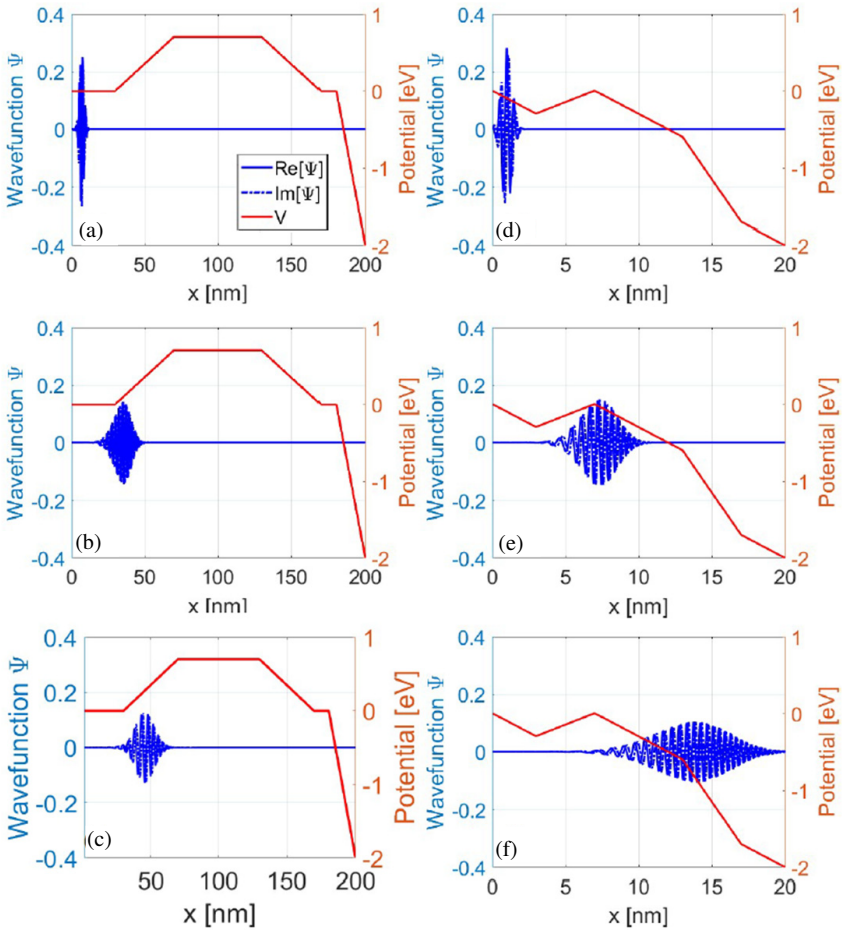

FIGURE 8. Electron propagation in a silicon based NMOS channel with different channel lengths at different time: (a) 200 nm at 0 fs, (b) 200 nm at 50 fs, (c) 200 nm at 150 fs, (d) 20 nm at 0 fs, (e) 20 nm at 5 fs, (f) 20 nm at 10 fs. The external drain-source and gate-source voltages $V_{GS} = 0$ V and $V_{DS} = 2$ V. Assume that the peak potential is 0.7 eV.

Figure 7 presents the IV characteristics of the 200-nm and 20-nm NMOS with various external voltage values V_{DS} and V_{GS}. These plots are obtained based on (26) using the algorithm shown in Section 3, where the corresponding potential distributions, transmission functions, and Fermi-Dirac distributions like those in Figs. 3–6 are calculated. It is observed

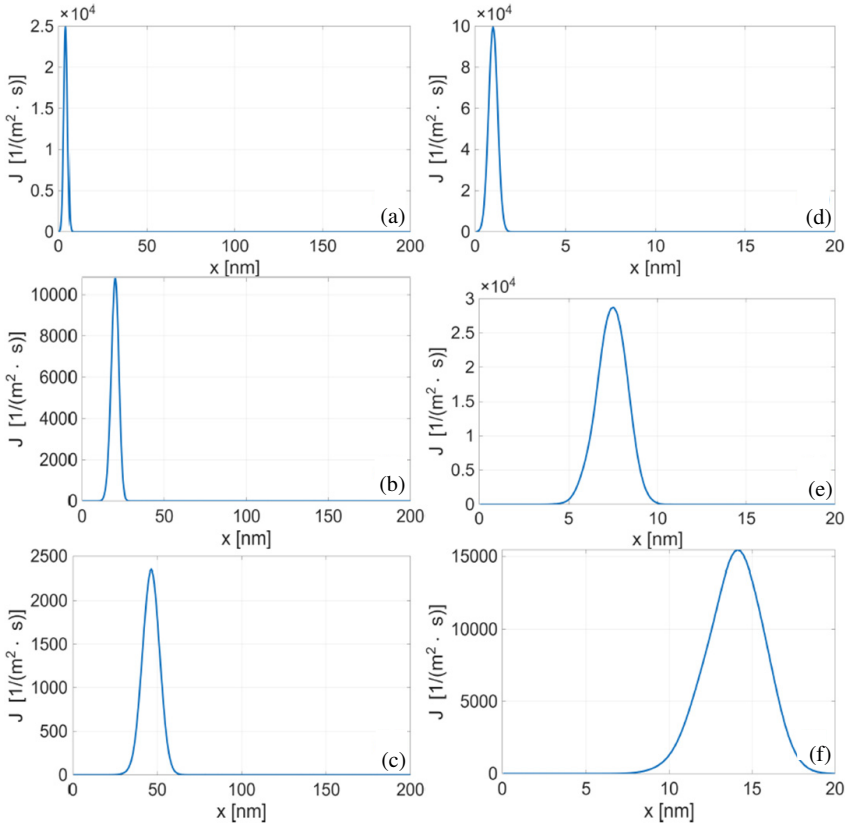

FIGURE 9. Probability current densities in 200 nm and 20 nm NMOS at different time. (a) 200 nm at $t = 0$ fs, (b) 200 nm at $t = 50$ fs, (c) 200 nm at $t = 150$ fs, (d) 20 nm at $t = 0$ fs, (e) 20 nm at $t = 5$ fs, and (f) 20 nm at $t = 10$ fs. The external drain-source and gate-source voltages $V_GS = 0$ V and $V_DS = 2$ V.

in Fig. 7(a) that there is no current formed in the channel when the gate-source voltage $V_{GS} = 0$ V. Since the barrier potential cannot be overcome in the NMOS with a channel length of 200 nm. For a small gate-source voltage V_{GS} of 0.2 V, the channel current is expected to be small due to the relatively high barrier potential and incomplete channel formation. When V_{GS} is increased to 0.7 V, the channel is completely formed, where the channel current rises with an increasing V_{DS} in the triode region and saturated to approximately 19.0 µA in the saturation region with $V_{DS} \geq 0.6$ V. However, when the channel length is reduced to 20 nm, the IV characteristic of the NMOS is fundamentally changed. Unlike the 200-nm NMOS, Fig. 7(b) shows that the gate-source voltage V_{GS} does not have a dominant impact on the channel current. When $V_{GS} = 0$ V, the current in the 20-nm NMOS can be increased to 18.4 µA with $V_{GS} = 2$ V, compared to no current in the cutoff mode of the 200-nm NMOS. The observed substantial current at $V_{GS} = 0$ V for a 20-nm channel arises from quantum mechanical barrier penetration and drain-induced barrier lowering under the condition of a short channel length and a nonzero V_{DS}. This demonstrates the difference in the cutoff modes of NMOS with different channel lengths. When $V_{GS} \geq 0.7$ V, the IV characteristics of the 20-nm and 200-nm NMOS are similar. To understand the difference in IV characteristics of different NMOS with small gate-source voltages $V_{GS} < 0.7$ V, the electron propagation using FDTD is investigated.

5.2. Electron Scattering Using the FDTD Solver

Figure 8 presents electron propagation as a wave packet in a silicon based 200-nm and 20-nm NMOS when $V_{GS} = 0$ V and $V_{DS} = 2$ V, which is obtained by (30a) and (30b) using the FDTD solver in Section 4. The solid and dashed blue lines represent the real and imaginary parts of the electron wavefunction, respectively, read from the vertical axis at the left-hand side. The solid red line presents the potential distribution in the channel, read from the vertical axis at the right-hand side. The wavefunction is a sinusoidal waveform in a Gaussian envelope, where $\psi(x) = e^{-(\frac{x-x_0}{\sigma})^2} e^{i \cdot 2\pi \frac{x-x_0}{\lambda}}$ with a center location of $x_0 = 4$ nm, a pulse width of $\sigma = 2$ nm, and a wavelength of $\lambda = 2$ nm. Figs. 8(a)–8(c) show the electron propagation in an NMOS with a 200 nm channel at 0, 50, and 150 fs. The initial location of the electron wavefunction is presented in Fig. 8(a). At 50 fs, it propagates towards the potential barrier in Fig. 9(b). At 150 fs, Fig. 8(c) presents that the wavefunction is propagating back towards its initial location rather than going through the potential barrier. This explains that the channel is not formed, and there is no current flowing through the NMOS from the drain to the source terminal when $V_{GS} = 0$ V in Fig. 7(a).

Figures 8(d)–8(f) present the electron propagation in an NMOS with a shorter 20 nm channel at 0, 5, and 10 fs. Due to the shorter channel length, the external drain-source voltage V_{DS} will lower the potential across the entire 20 nm chan-

nel. Fig. 8(d) shows the initialized electron wavefunction at the source terminal of the NMOS, which propagates into the potential barrier in Fig. 8(e) and arrives at the right-hand side of the channel at the drain terminal in Fig. 8(f). The electron is propagating forward through the potential barrier. This indicates that the channel is formed, and currents will flow from the drain to the source terminal, which is in the opposite direction of the electron propagation from the source to the drain terminal. The electron propagating through the channel leads to the current flow, explaining the IV characteristics of the short NMOS when $V_{GS} = 0\,\text{V}$ and $V_{DS} \geq 0.5\,\text{V}$ in Fig. 7(b).

Figure 9 shows probability current densities in 200-nm and 20-nm NMOS when $V_{GS} = 0\,\text{V}$ and $V_{DS} = 2\,\text{V}$, which is obtained by the probability current density equation $J(x,t)$ under (4). As the electron travels in the NMOS channel, the spatial distribution of the probability current density changes as well. Figs. 9(a)–9(c) show probability current densities in the 200-nm NMOS channel at 0, 50, and 150 fs. Due to a high potential barrier in Fig. 9(a), the electron is scattered back to the source terminal and fails to tunnel through. Figs. 9(d)–9(f) show probability current densities in the 20-nm NMOS channel at 0, 5, and 10 fs. Due to drain-induced barrier lowering in the short 20-nm channel, the electron tunnels through the channel and arrives at the drain terminal, creating current flow. To verify the conservation of energy, the total energy of the electron in the 200-nm NMOS is a constant of 0.34 eV, and that in the 20-nm NMOS is a constant of 5.42 eV, which do not vary with time.

6. CONCLUSION

Unlike the conventional algorithm to implement NEGF in quantum transport and FDTD in observing electron scattering independently, NEGF and FDTD are combined to achieve a hybrid quantum transport algorithm based on the Schrödinger equation. In the NEGF solver, the transmission function and Fermi-Dirac distributions are used to obtain channel currents in nanoscale MOSFETs. To understand the difference in IV characteristics of NMOS with different channel lengths, the FDTD solver is applied to obtain the time-domain response of the electron wave packet with the presence of different potential distributions. The different potential distributions across the channel lead to differences in transmission functions when all NMOS parameters are the same except for the channel length. This results in electron back propagating (no current) in a long channel and forward propagating (current flow) in a short channel under certain external drain-source and gate-source voltages. The future work will focus on developing a fully coupled NEGF-FDTD self-consistent formulation where the electron wavefunction dynamically interacts with quantum transport. Full NEGF-Poisson simulations will be considered as well to quantify bias-induced channel potential redistribution.

APPENDIX A. THE SPECTRAL AND GREEN'S FUNCTION

The spectral function (13) presents the energy distribution and density of states in a channel, which is broadened due to the presence of external leads or reservoirs. Instead of using delta functions, the diagonal eigenstate representation can be written as [36],

$$A(E) = 2\pi \begin{bmatrix} \frac{\frac{\gamma_1}{2\pi}}{(\gamma_1/2)^2+(E-\varepsilon_1)^2} & \cdots & 0 \\ \vdots & \ddots & \vdots \\ 0 & \cdots & \frac{\frac{\gamma_N}{2\pi}}{(\gamma_N/2)^2+(E-\varepsilon_N)^2} \end{bmatrix} \tag{A1}$$

where γ_n is an introduced loss term with n from 1 to N, contributing to broadening, and N is the total number of discretized cells of the channel in a MOSFET. To represent the spectral function A in terms of the Green's function G and find the relation (14) through the corresponding matrix forms, the derivation of the Green's function is visited.

The matrix version of the time-independent Schrödinger equation (16) with external DC voltage sources can be expressed by,

$$[IE - H]\,\psi = f \tag{A2}$$

where the column-vector state variable ψ can be written as a superposition of eigenfunctions Φ with column-vector complex coefficients c, $\psi = \Phi c$, and similarly, the forcing function f can be written as a superposition of the same eigenfunctions with another set of column-vector complex coefficients d, $f = \Phi d$. Substitute $\psi = \Phi c$ and $f = \Phi d$ into (32) and multiply from the left by the Hermitian conjugate of Φ at both sides of the equation, resulting in,

$$\Phi^{\dagger}\,[IE - H]\,\Phi c = d \tag{A3}$$

Therefore, the complex coefficients c can be represented by,

$$c = G\,(E)\,d \tag{A4}$$

where the Green's function is defined as,

$$G\,(E) = \left\{\Phi^{\dagger}\,[IE - H]\,\Phi\right\}^{-1} \tag{A5}$$

Due to the unitary property of the eigenfunctions Φ, (35) is further reduced to a diagonal matrix by adding a loss term $i\gamma_n/2$, which is similar to (15),

$$G(E) = 2\pi \begin{bmatrix} \frac{1}{E-\varepsilon_1+i\gamma_1/2} & \cdots & 0 \\ \vdots & \ddots & \vdots \\ 0 & \cdots & \frac{1}{E-\varepsilon_N+i\gamma_N/2} \end{bmatrix} \tag{A6}$$

The relation between the spectral function and the Green's function $A(E) = i[G(E) - G^{\dagger}(E)]$ in (14) can be found by connecting (31) and (36). Note that there is a difference in loss terms of (15) and (36). In (15), the boundaries between the channel and the external reservoirs in practical MOSFETs are considered [36].

APPENDIX B. THE HAMILTONIAN AND SELF-ENERGY MATRICES

To obtain the channel current (26) in a semiconductor device, the Green's function in (15) is needed to calculate the transmission matrix, which leads to the calculation of the Hamiltonian operator H. Based on the second-order spatial derivative

from FDTD without considering the time derivative, the time-independent Schrödinger equation (16) can be expressed by the corresponding time-difference form,

$$H\psi_n = -\chi_0\psi_{n+1} + (2\chi_0 + V_n)\,\psi_n - \chi_0\psi_{n-1} \tag{B1}$$

where the constant $\chi_0 = \frac{\hbar^2}{2m_e\Delta x^2}$, and V_n is the potential in the nth spatial cell of the MOSFET channel with $n = 1 : N$. This leads to the sparse Hamiltonian matrix in quantum transport $H = T+V$, which is a combination of kinetic and potential matrices,

$$T = \chi_0 \begin{bmatrix} 2 & -1 & 0 & \cdots & 0 & 0 \\ -1 & 2 & -1 & 0 & \cdots & 0 \\ 0 & -1 & 2 & -1 & 0 & \vdots \\ \vdots & 0 & \ddots & \ddots & \ddots & 0 \\ 0 & \cdots & 0 & -1 & 2 & -1 \\ 0 & 0 & \cdots & 0 & -1 & 2 \end{bmatrix} \tag{B2}$$

$$V = \begin{bmatrix} V_1 & 0 & 0 & \cdots & 0 & 0 \\ 0 & V_2 & 0 & 0 & \cdots & 0 \\ 0 & 0 & V_3 & 0 & 0 & \vdots \\ \vdots & 0 & \ddots & \ddots & \ddots & 0 \\ 0 & \cdots & 0 & 0 & V_{N-1} & 0 \\ 0 & 0 & \cdots & 0 & 0 & V_N \end{bmatrix} \tag{B3}$$

where the $N \times N$ potential matrix V is purely diagonal. The $N \times N$ sparse kinetic matrix T has diagonal, superdiagonal, and subdiagonal elements. N is the total number of discretized spatial cells of the channel in a MOSFET. Observe that the first and last rows of the kinetic matrix T have two rather than three nonzero elements because of two ends of the channel. To consider electron wavefunction propagating through the two boundaries between the external reservoirs and the MOSFET channel, the self-energy matrix Σ in (17) is involved in the Green's function (15).

Assuming that an electron propagates through the left-hand side of the channel into the source in Fig. 1, at the first cell $n = 1$ in the channel next to the boundary, (37) shows that the wavefunction ψ_1 satisfies,

$$H\psi_1 = -\chi_0\psi_2 + (2\chi_0 + V_1)\,\psi_1 - \chi_0\psi_0 \tag{B4}$$

where ψ_0 represents the wavefunction at the cell $n = 0$ in the source next to the boundary, and ψ_2 represents the wavefunction at the cell $n = 2$ on the right-hand side of the 1st cell. Since $n = 0$ is out of the bound of the Hamiltonian matrix, a remedy to the term ψ_0 is needed, which can be related to ψ_1 through $\psi_0 = \frac{\psi_0}{\psi_1}\psi_1$. Based on the plane wave assumption, the discretized time-independent wave function at the left end of the channel in Fig. 1 can be written as,

$$\psi_n = e^{-i\cdot k_1\cdot n\Delta x} \tag{B5}$$

leading to $\frac{\psi_0}{\psi_1} = e^{i\cdot k_1\Delta x}$. The last term in (39) is modified to $-\chi_0 e^{i\cdot k_1\Delta x}\psi_1$ with a coefficient of $-\chi_0 e^{i\cdot k_1\Delta x}$, which is the element in top left corner of the self-energy matrix in (17). Similarly, at the right end of the channel in Fig. 1, the electron propagates through the right-hand side of the channel into the drain. The term $-\chi_0\psi_{N+1}$ is modified to $-\chi_0 e^{i\cdot k_2\Delta x}\psi_N$ with a coefficient of $-\chi_0 e^{i\cdot k_2\Delta x}$, which is the element in bottom right corner of the self-energy matrix.

REFERENCES

[1] Moore, G. E., "Cramming more components onto integrated circuits," *Electronics*, Vol. 38, No. 8, 1965.

[2] Moore, G. E., "Lithography and the future of Moore's law," *IEEE Solid-State Circuits Society Newsletter*, Vol. 11, No. 3, 37–42, 2006.

[3] Fowler, R. H. and L. Nordheim, "Electron emission in intense electric fields," *Proc. R. Soc. A*, Vol. 119, No. 781, 173–181, May 1928.

[4] Lenzlinger, M. and E. H. Snow, "Fowler-Nordheim tunneling into thermally grown SiO_2," *IEEE Transactions on Electron Devices*, Vol. 15, No. 9, 686–686, Sep. 1968.

[5] Fowler, A. B., G. L. Timp, J. J. Wainer, and R. A. Webb, "Observation of resonant tunneling in silicon inversion layers," *Physical Review Letters*, Vol. 57, No. 1, 138–141, 1986.

[6] Zhou, J.-R. and D. K. Ferry, "Simulation of ultra-small GaAs MESFET using quantum moment equations," *IEEE Transactions on Electron Devices*, Vol. 39, No. 3, 473–478, Mar. 1992.

[7] Degond, P. and A. E. Ayyadi, "A coupled Schrödinger drift-diffusion model for quantum semiconductor device simulations," *Journal of Computational Physics*, Vol. 181, No. 1, 222–259, Sep. 2002.

[8] Grasser, T., T.-W. Tang, H. Kosina, and S. Selberherr, "A review of hydrodynamic and energy-transport models for semiconductor device simulation," *Proceedings of the IEEE*, Vol. 91, No. 2, 251–274, Feb. 2003.

[9] De Falco, C., E. Gatti, A. L. Lacaita, and R. Sacco, "Quantum-corrected drift-diffusion models for transport in semiconductor devices," *Journal of Computational Physics*, Vol. 204, No. 2, 533–561, Apr. 2005.

[10] Ahn, C. and M. Shin, "Ballistic quantum transport in nanoscale schottky-barrier tunnel transistors," *IEEE Transactions on Nanotechnology*, Vol. 5, No. 3, 278–283, May 2006.

[11] Yang, T.-Y., A. Ruffino, J. Michniewicz, Y. Peng, E. Charbon, and M. F. Gonzalez-Zalba, "Quantum transport in 40-nm MOSFETs at deep-cryogenic temperatures," *IEEE Electron Device Letters*, Vol. 41, No. 7, 981–984, 2020.

[12] Chen, Y., Y. Zhang, J. Huang, J. Xu, C. Luo, and G. Guo, "Compact modeling of quantum transport in 55-nm MOSFETs at cryogenic temperatures," *IEEE Electron Device Letters*, Vol. 44, No. 9, 1392–1395, Sep. 2023.

[13] Ferry, D. K., J. Weinbub, M. Nedjalkov, and S. Selberherr, "A review of quantum transport in field-effect transistors," *Semiconductor Science and Technology*, Vol. 37, No. 4, 043001, 2022.

[14] Baym, G. and L. P. Kadanoff, "Conservation laws and correlation functions," *Physical Review*, Vol. 124, No. 2, 287, Oct. 1961.

[15] Keldysh, L. V., "Diagram technique for nonequilibrium processes," *Soviet Phys. JETP*, Vol. 20, No. 4, 1018–1026, 1965.

[16] Danielewicz, P., "Quantum theory of nonequilibrium processes, I," *Annals of Physics*, Vol. 152, No. 2, 239–304, 1984.

[17] Meir, Y. and N. S. Wingreen, "Landauer formula for the current through an interacting electron region," *Physical Review Letters*, Vol. 68, No. 16, 2512, Apr. 1992.

[18] Venugopal, R., Z. Ren, S. Datta, M. S. Lundstrom, and D. Jovanovic, "Simulating quantum transport in nanoscale transistors: Real versus mode-space approaches," *Journal of Applied Physics*, Vol. 92, No. 7, 3730–3739, Oct. 2002.

[19] Jiménez, D., B. Iñíguez, J. Suñé, and J. J. Sáenz, "Analog performance of the nanoscale double-gate metal-oxide-semiconductor field-effect-transistor near the ultimate scaling limits," *Journal of Applied Physics*, Vol. 96, No. 9, 5271–5276, Nov. 2004.

[20] Arefinia, Z., "Nonequilibrium Green's function treatment of a new nanoscale dual-material double-gate MOSFET," *Physica E: Low-dimensional Systems and Nanostructures*, Vol. 43, No. 5, 1105–1110, Mar. 2011.

[21] Khan, H. R., D. Mamaluy, and D. Vasileska, "3D NEGF quantum transport simulator for modeling ballistic transport in nano FinFETs," *Journal of Physics: Conference Series*, Vol. 107, No. 1, 012007, 2008.

[22] Lansbergen, G. P., R. Rahman, C. J. Wellard, I. Woo, J. Caro, N. Collaert, S. Biesemans, G. Klimeck, L. C. L. Hollenberg, and S. Rogge, "Gate-induced quantum-confinement transition of a single dopant atom in a silicon FinFET," *Nature Physics*, Vol. 4, No. 8, 656–661, Aug. 2008.

[23] Martinez, A., A. Price, R. Valin, M. Aldegunde, and J. Barker, "Impact of phonon scattering in Si/GaAs/InGaAs nanowires and FinFets: A NEGF perspective," *Journal of Computational Electronics*, Vol. 15, No. 4, 1130–1147, 2016.

[24] Bousari, N. B., M. K. Anvarifard, and S. Haji-Nasiri, "Benefitting from high-κ spacer engineering in balistic triple-gate junctionless FinFET — A full quantum study," *Silicon*, Vol. 12, No. 9, 2221–2228, 2020.

[25] Mech, B. C., K. Koley, and J. Kumar, "The understanding of SiNR and GNR TFETs for analog and RF application with variation of drain-doping molar fraction," *IEEE Transactions on Electron Devices*, Vol. 65, No. 10, 4694–4700, Oct. 2018.

[26] M'foukh, A., M. G. Pala, and D. Esseni, "Full-band quantum transport of heterojunction electron devices with empirical pseudopotentials," *IEEE Transactions on Electron Devices*, Vol. 67, No. 12, 5662–5668, Dec. 2020.

[27] Berrada, S., H. Carrillo-Nunez, J. Lee, C. Medina-Bailon, T. Dutta, O. Badami, F. Adamu-Lema, V. Thirunavukkarasu, V. Georgiev, and A. Asenov, "Nano-electronic Simulation Software (NESS): A flexible nano-device simulation platform," *Journal of Computational Electronics*, Vol. 19, No. 3, 1031–1046, 2020.

[28] Mil'nikov, G., J.-I. Iwata, N. Mori, and A. Oshiyama, "RSDFT-NEGF transport simulations in realistic nanoscale transistors," *Journal of Computational Electronics*, Vol. 22, No. 5, 1181–1201, 2023.

[29] Zhu, J., J. Cao, C. Song, B. Li, and Z. Han, "Numerical investigation on the convergence of self-consistent Schrödinger-Poisson equations in semiconductor device transport simulation," *Nanotechnology*, Vol. 35, No. 31, 315001, May 2024.

[30] Zhu, J., J. Cao, C. Song, B. Li, and Z. Han, "Jiezi: An open-source Python software for simulating quantum transport based on non-equilibrium Green's function formalism," *Computer Physics Communications*, Vol. 302, 109251, 2024.

[31] Zou, J., Z. Zhouyin, D. Lin, Y. Huang, L. Zhang, S. Hou, and Q. Gu, "Deep learning accelerated quantum transport simulations in nanoelectronics: From break junctions to field-effect transistors," *NPJ Computational Materials*, Vol. 11, 375, 2025.

[32] Vecil, F., J. M. Mantas, and P. Alonso-Jordá, "Efficient GPU implementation of a Boltzmann-Schrödinger-Poisson solver for the simulation of nanoscale DG MOSFETs," *The Journal of Supercomputing*, Vol. 79, No. 12, 13 370–13 401, 2023.

[33] Zhu, X. and H. Yin, "Hybrid simulation method of quantum characteristics for advanced Si MOSFETs under extreme conditions by incorporating simplified master equation with TCAD," *Results in Physics*, Vol. 63, 107856, Aug. 2024.

[34] Espiñeira, G., A. J. García-Loureiro, and N. Seoane, "Parallel approach of Schrödinger-based quantum corrections for ultrascaled semiconductor devices," *Journal of Computational Electronics*, Vol. 21, 10–20, 2022.

[35] Kim, K. Y., H.-H. Park, S. Jin, U. Kwon, W. Choi, and D. S. Kim, "Quantum transport through a constriction in nanosheet gate-all-around transistors," *Communications Engineering*, Vol. 4, No. 1, 92, 2025.

[36] Datta, S., *Quantum Transport: Atom to Transistor*, Cambridge University Press, New York, NY, 2005.

[37] Visscher, P. B., "A fast explicit algorithm for the time-dependent Schrödinger equation," *Computers in Physics*, Vol. 5, No. 6, 596–598, Nov. 1991.

[38] Sullivan, D. M. and D. S. Citrin, "Determination of the eigenfunctions of arbitrary nanostructures using time domain simulation," *Journal of Applied Physics*, Vol. 91, No. 5, 3219–3226, Mar. 2002.

[39] Sullivan, D. M. and D. S. Citrin, "Determining quantum eigenfunctions in three-dimensional nanoscale structures," *Journal of Applied Physics*, Vol. 97, No. 10, 104305, May 2005.

[40] Soriano, A., E. A. Navarro, J. A. Portí, and V. Such, "Analysis of the finite difference time domain technique to solve the Schrödinger equation for quantum devices," *Journal of Applied Physics*, Vol. 95, No. 12, 8011–8018, Jun. 2004.

[41] Nagel, J. R., "A review and application of the finite-difference time-domain algorithm applied to the Schrödinger equation," *Applied Computational Electromagnetics Society Journal (ACES)*, Vol. 24, No. 1, 1–8, Jun. 2022.

[42] Sullivan, D. M., S. Mossman, and M. G. Kuzyk, "Time-domain simulation of three dimensional quantum wires," *PLoS ONE*, Vol. 11, No. 4, e0153802, 2016.

[43] Decleer, P., A. Van Londersele, H. Rogier, and D. V. Ginste, "Nonuniform and higher-order FDTD methods for the Schrödinger equation," *Journal of Computational and Applied Mathematics*, Vol. 381, 113023, Jan. 2021.

[44] Bekmambetova, F. and P. Triverio, "Calculation and conservation of probability and energy in the numerical solution of the Schrödinger equation with the finite-difference time-domain method," *IEEE Transactions on Microwave Theory and Techniques*, Vol. 72, No. 4, 2110–2129, Apr. 2024.

[45] Du, K., S. He, C. Zhao, N. Liu, and Q. H. Liu, "A 3-D spectral element time-domain method with perfectly matched layers for transient Schrödinger equation," *IEEE Journal on Multiscale and Multiphysics Computational Techniques*, Vol. 9, 188–197, 2024.

[46] Tan, E. L. and D. Y. Heh, "Critical-point-based stability analyses of finite-difference time-domain methods for Schrödinger equation incorporating vector and scalar potentials," *IEEE Journal on Multiscale and Multiphysics Computational Techniques*, Vol. 10, 38–46, 2025.

[47] Ren, K., "FDTD in computational electromagnetics and quantum transport," in *2025 United States National Committee of URSI National Radio Science Meeting (USNC-URSI NRSM)*, 16–17, Boulder, CO, USA, Jan. 2025.